https://doi.org/10.5194/egusphere-2026-4971
Preprint. Discussion started: 8 September 2026

Stratospheric regulation of planetary wave evolution and surface impacts during the 2019 Southern Hemisphere sudden stratospheric warming

Kexiang Feng[1], Jian Rao[1, *], Chaim I. Garfinkel[2], Amy H. Butler[3], Blanca Ayarzagüena[4,5], and Xiaoqi Zhang[1]

[1]State Key Laboratory of Environment Characteristics and Effects for Near-space, Nanjing University of Information Science and Technology, Nanjing 210044, China

[2]Fredy and Nadine Herrmann Institute of Earth Sciences, The Hebrew University of Jerusalem, Givat Ram, Jerusalem, Israel

[3]Chemical Sciences Laboratory, National Oceanic and Atmospheric Administration, Boulder, CO, United States

[4]Department of Earth Physics and Astrophysics, Facultad de CC. Físicas, Universidad Complutense Madrid, Madrid, Spain

[5]Instituto de Geociencias, Consejo Superior de Investigaciones Científicas – Universidad Complutense de Madrid (CSIC-UCM), Madrid, Spain.

*Correspondence: Dr. Jian Rao, raojian@nuist.edu.cn

https://doi.org/10.5194/egusphere-2026-4971
Preprint. Discussion started: 8 September 2026

Abstract

The role of the stratospheric state in regulating planetary wave activity during sudden stratospheric warming (SSW) events and subsequent surface impacts is still not well understood. Using multiple subseasonal-to-seasonal (S2S) forecast models from the Stratospheric Nudging and Predictable Surface Impacts (SNAPSI) framework, we investigate the 2019 Southern Hemisphere SSW through both free forecasts and stratospheric sensitivity experiments. In the control and nudged experiments, the stratospheric state is constrained toward the zonally symmetric circulation climatology and the observed real-time evolution, respectively, allowing the stratospheric contribution to wave evolution and surface responses to be isolated. Forecasts show that biases in planetary wave activity arise from different processes during different stages of the event. In the early stage, underestimated tropospheric forcing dominates the weak upward wave propagation. However, during the central stage, upper-stratospheric wave activity biases are further regulated by the stratospheric state through changes in the critical line. Moreover, the nudged stratosphere induced a weak but detectable enhanced tropospheric favorable pattern. These results highlight that the stratosphere is not only a passive responder to tropospheric wave forcing but also actively regulates planetary wave evolution. Diagnosis of the three-dimensional wave activity flux (WAF) further reveals a zonally asymmetric downward stratospheric signal in early October, which is forecast in the nudged minus control experiments but with a farther westward shift than observed. Models tend to forecast an earlier than observed negative Southern Annular Mode (SAM)-like pattern in the troposphere and stronger regional precipitation contrasts in the nudged minus control experiments. Several models simulate significantly drier responses in eastern Australia following the downward-propagating SAM in the nudged experiments, while the remaining models show a more dominant role for the lower troposphere. In contrast, the near-surface impacts over South America show large inter-model spread in the nudged experiments, possibly due to the westward-biased forecasts of downward WAF in models.

https://doi.org/10.5194/egusphere-2026-4971
Preprint. Discussion started: 8 September 2026

1 Introduction

Sudden stratospheric warming (SSW) events are the most intense disturbance in the polar stratosphere, predominantly driven by anomalous upward propagation of planetary waves (Baldwin and Dunkerton, 2001; Baldwin et al., 2021; Rao et al., 2018). The substantial heat flux and easterly momentum transported by the wave activity from the lower atmosphere accumulate to result in dramatic warming in the middle and upper polar stratosphere and even reversal of zonal winds at 10 hPa and 60° latitude (U1060) (Butler et al., 2015; Butler and Gerber, 2018; Chwat et al., 2022; Feng et al., 2025). In the Northern Hemisphere (NH), SSW occurs 6 or 7 times every 10 years, with typical events leading to a rapid U1060 decline of 40-50 m/s and a reversal (Charlton and Polvani, 2007; Rao et al., 2025). In the Southern Hemisphere (SH), only one SSW event in the observational record (in 2002) led to the reversal of U1060 (Allen et al., 2003; Newman and Nash, 2005; Rao et al., 2020b; Lim et al., 2021), and another one in September 2019 led to a decline in U1060 of over 60 m/s but ultimately failed to generate a wind reversal (only drops below the 20 m/s isotach) (Lim et al., 2021; Rao et al., 2020b; Liu et al., 2022; Feng et al., 2025). Although the 2019 SH SSW event is commonly classified as a "minor" SSW in literature, it is characterized by several unique features and the subsequent impacts are far from "minor". For example, the preconditioned tropospheric wave forcing in 2019 showed the longest persistence on record, and the ozone concentrations were also the highest (Noguchi et al., 2020; Shen et al., 2020; Jucker and Goyal, 2022; Ma et al., 2022). Exceptionally, the total U1060 deceleration in the 2019 SH SSW exceeds most NH SSW events. Further, the 2019 SH SSW event also produced the strongest negative phase of Southern Annular Mode (SAM) on record, which coupled downward to the surface and persisted for over two months until the end of austral late spring (Lim et al., 2021; Feng et al., 2025; Purich et al., 2026). Previous studies have demonstrated that such an extreme and prolonged negative SAM event is associated with the extreme warming over Antarctica and subsequent wildfire weather over Australia (Lim et al., 2019; Lim et al., 2021; Feng et al., 2025).

Given the exceptionality of the 2019 SH SSW event, analyzing and predicting it using model-based approaches has become the most practical and feasible strategy. Using the

https://doi.org/10.5194/egusphere-2026-4971
Preprint. Discussion started: 8 September 2026

subseasonal to seasonal (S2S) database, Rao et al. (2020b) reported that the forecast window of this event was about 18 days for some high skill models, longer than the average predictive limit of 1-2 weeks for NH SSWs (Rao et al., 2019; Rao et al., 2020a). Certain precursor conditions in mid-to-late 2019, such as the easterly phase of the quasi-biennial oscillation (QBO), which eventually developed into the 2019/20 QBO disruption (Wang et al., 2023), and a positive Indian Ocean Dipole (IOD), were favorable for the occurrence of this SH SSW event (Rao et al., 2020b). However, some of these factors, such as the positive IOD and the moderate central Pacific El Niño, may also complicate the attribution of the downward impacts of this SSW event (Cai et al., 2011; Liguori et al., 2022; Reddy et al., 2022). It remains uncertain whether the surface impacts are causally forced from the stratosphere, and it is also unclear whether model biases in the stratospheric state can degrade prediction of the dynamical processes during the SSW events. .

To investigate the stratospheric role in the wave dynamics and attribute the surface impacts to stratospheric disturbances, the Stratospheric Nudging And Predictable Surface Impacts (SNAPSI) protocol was designed in 2022 (Hitchcock et al., 2022). The SNAPSI protocol chooses three recent SSW events (2018 NH SSW, 2019 NH SSW, and 2019 SH SSW) for case studies. Using zonally symmetric stratospheric nudging, the internally generated planetary wave activity, which is crucial for stratosphere-troposphere coupling, is only weakly constrained and remains largely free to evolve. Based on this technique, the protocol aims at providing three basic experiments: free, control, and nudged. The free experiment refers to a forecast without any artificial constraints or nudging. In the control and nudged experiments, the stratosphere is nudged towards either the time-evolving reanalysis climatology or the actual reanalysis evolution in 2019, respectively. The nudging is applied gradually starting at 90 hPa, and the maximum amplitude is reached at and above 50 hPa. All three experiments contain large ensembles, which helps to increase the statistical robustness and to isolate the dynamically forced signals.

Benefiting from the SNAPSI protocol, several studies have provided valuable insight on SSW events. For example, during the 2018 NH SSW event, improved representation of the stratospheric state enhances forecasts of the persistent negative North Atlantic Oscillation

https://doi.org/10.5194/egusphere-2026-4971
Preprint. Discussion started: 8 September 2026

(NAO) and subsequent extreme precipitation over the Iberian Peninsula (Dai et al., 2025; Lee et al., 2025); however, nudging the stratosphere failed to improve the forecasts of the negative Pacific/North American pattern (PNA), which mainly results from the weakness of simulating mid-latitude dynamical processes and poor representation of the tropospheric precursors (Huang et al., 2026). During the 2019 NH SSW event, stratospheric forcing degraded midlatitude forecast skill, likely due to overestimated stratosphere-troposphere coupling and insufficient representation of tropics-extratropics teleconnections in the troposphere (Lee et al., 2025). In the 2019 SH case, nudging the zonal-mean stratosphere did not recover the full strength of the observed downward negative SAM signal, and the polar vortex exhibited a significant zonally asymmetric structure, which is demonstrated to be crucial for forecasting the Australian hot and dry conditions (Feng et al., 2025; Seviour et al., 2026).

It is worth noting that, despite these SNAPSI-based studies on surface impacts, substantial scope for further investigation still remains. For example, Ayarzagüena et al. (2026) have showed that the downward influence of the pre-SSW stratospheric state on wave activities is relatively weak across the three SNAPSI cases. Although there were some hints of a relevant modulation by the stratospheric state of the wave evolution during the 2019 SH SSW, this modulation still remains insufficiently explored. Moreover, previous studies have mainly identified the timing of surface impacts based on the downward propagation of the negative SAM signal, which gives only a zonal mean perspective. Here, we provide a three-dimensional perspective, suggesting that stratospheric influences on the surface weather may emerge earlier through a zonally asymmetric process, or may emerge at some latitudes first (Garfinkel et al 2023). Given the rarity of SH SSWs, exploiting SNAPSI experiments to evaluate the forecast performance of the 2019 SH SSW and diagnose its sources of bias is of great importance for improving our understanding of SH SSW characteristics and advancing model prediction capability. Therefore, in the following sections, we seek to answer the following questions: How skillful are free-running SNAPSI models in capturing the 2019 SH SSW (Sect. 3)? How well do the models represent the tropospheric wave forcing, and how was the wave activity affected by the stratospheric state during the SSW event (Sect. 4)? Is there evidence of stratospheric impacts on surface weather prior to the downward propagation of the negative

https://doi.org/10.5194/egusphere-2026-4971
Preprint. Discussion started: 8 September 2026

SAM signal in early October 2019? (Sect. 5)? Section 2 describes the data and methodology used in this study. The last section gives the summary and discussion.

2 Data and Methodology

2.1 SNAPSI models and reanalysis

In the SNAPSI zonally symmetric nudging configuration, only the zonal-mean temperature and zonal wind are relaxed toward the reference state. ERA5 (Hersbach et al., 2020) is the sole reanalysis dataset prescribed as the reference state for stratospheric nudging, and the corresponding climatological reference is also derived from ERA5 6-hour means over 1st July 1979 to 30 June 2019, rather than from a model climatology (Hitchcock et al., 2022). Accordingly, the ERA5 reanalysis from 1st July 1979 to 30 June 2019 are used as the baseline to calculate the model biases in this study.

According to the SNAPSI experimental design, each case includes two initialization dates with 45-day forecasts to capture both SSW evolution and subsequent surface impacts, as well as to assess the benefit of reduced lead time. For the 2019 SH SSW, the lagged downward propagation of the negative SAM signal exceeded one month (e.g. Lim et al., 2021), and the second initialization (1 October) does not cover the SSW onset. We therefore use only the first initialization (29 August) to study the SSW evolution forecasts, corresponding to a forecast period from 29 August to 12 October 2019, with model output every 6 hours. Six SNAPSI models are used in this study. They are from CNR-ISAC (GLOBO) (Mastrangelo and Malguzzi, 2019), ECMWF (IFS) (ECMWF, 2016), KMA(GloSea6-KMA) (Williams et al., 2015), Meteo-France (CNRM-CM6-1) (Voldoire et al., 2019), SNU(GRIMs) (Koo et al., 2023), and UKMO (GloSea6-UKMO) (MacLachlan et al., 2015). All models have a model top at or above 0.1 hPa (except CNR-ISAC; its model top is 6.8 hPa) and an ensemble size of 50 members. Further details can also be found in Lee et al. (2025).

2.2 Methods

2.2.1 Identification of 2019 SH SSW

It has been reported that the 2019 SH SSW did not lead to a reversal of U1060. However, according to Rao et al. (2020b), the zonal-mean zonal wind at 10 hPa and 50°S reversed on 15

https://doi.org/10.5194/egusphere-2026-4971
Preprint. Discussion started: 8 September 2026

September, which coincided with U1060 dropping below 20 m/s. Therefore, a looser SSW definition is used in this study: the SSW onset is defined as the first time when U1060 falls below 20 m/s, consistent with definitions widely used in previous studies.

2.2.2 Identification of tropospheric favorable pattern

Ayarzagüena et al. (2026) have shown that the favorable wave source during this SSW occurred at the location of the climatological WN1 pattern (ridge, 45°S–75°S, 60°W–160°W; and trough, 45°S–75°S, 20°E–120°E), as alignment of an anomalous wave with climatology can lead to constructive wave interference and enhancement of wave activity (Smith and Kushner, 2012). Here, we follow this definition. The favorable pattern strength is obtained by calculating the absolute value of 500 hPa geopotential height anomaly within the climatological WN1 ridge and trough regions separately and then average the two values. For the models, the anomalies are also calculated relative to the daily-mean ERA5 reanalysis climatology.

2.2.3 Wave activity analysis

The Eliassen-Palm flux (EPF, **F**) (Edmon et al., 1980) (Equation 1) is related to the group speed of planetary waves, which can represent the propagation of the wave packet.

$$\mathbf{F} = a\cos\varphi \times \begin{pmatrix} -\overline{u'v'} \\ f\dfrac{\overline{\theta'v'}}{\overline{\theta}_p} \end{pmatrix}, \tag{1}$$

$$\nabla\cdot\mathbf{F} = \frac{1}{a\cos\varphi}\frac{\partial}{\partial\varphi}\left(F_{(\varphi)}\cos\varphi\right) + \frac{\partial}{\partial p}\left(F_{(p)}\right). \tag{2}$$

In the formulas, a, f, φ are the Earth radius, Coriolis parameter, and latitude, respectively. u, v, θ are zonal wind, meridional wind, and potential temperature, respectively. The overbar and superscript apostrophe denote the zonal mean and the deviation from the zonal mean, respectively. The subscript p represents the partial derivative with respect to pressure. When plotted, $F_{(\varphi)}$ and $F_{(p)}$ are scaled by dividing by πa and 10^5 Pa, respectively. $\nabla\cdot\mathbf{F}$ (Equation 2) is multiplied by 86400 to convert its unit to m s^{-1} d^{-1}.

To obtain a more comprehensive view of wave activity diagnostics, Plumb (1985) derived a three-dimensional formulation of the wave activity flux (WAF, **W**) (Equations 5, 6).

https://doi.org/10.5194/egusphere-2026-4971
Preprint. Discussion started: 8 September 2026

$$\mathbf{W}=\frac{p}{p_0}\cos\varphi\times\begin{pmatrix} v'^2-\dfrac{1}{2\Omega a\sin 2\varphi}\dfrac{\partial(v'\phi')}{\partial\lambda} \\ -u'v'+\dfrac{1}{2\Omega a\sin 2\varphi}\dfrac{\partial(u'\phi')}{\partial\lambda} \\ \dfrac{f}{S}\left[v'T'-\dfrac{1}{2\Omega a\sin 2\varphi}\dfrac{\partial(T'\phi')}{\partial\lambda}\right]\end{pmatrix}, \tag{5}$$

$$S=\frac{\partial\overline{T}}{\partial z}+\frac{\kappa\overline{T}}{H}. \tag{6}$$

In the formulas, p_0=1000 hPa, $\kappa\approx0.286$. Ω,λ,H,ϕ,T are the Earth's angular velocity, longitude, height scale, geopotential, and air temperature, respectively. All other symbols are standard.

The refractive index (RI, n^2) (Weinberger et al., 2021) (Equations 7, 8) is widely used to characterize the background for wave propagation, with waves tending to refract from negative toward positive regions.

$$n^2=\frac{\overline{q_\varphi}}{a\bar{u}}-\frac{s^2}{a^2\cos^2\varphi}-\frac{f^2}{4N^2H^2}, \tag{7}$$

$$\overline{q_\varphi}=2\Omega\cos\varphi-\frac{\partial}{\partial\varphi}\frac{\frac{\partial}{\partial\varphi}(\bar{u}\cos\varphi)}{a\cos\varphi}-\frac{af^2}{\rho_0}\frac{\partial}{\partial z}\left(\frac{\rho_0}{N^2}\frac{\partial\bar{u}}{\partial z}\right). \tag{8}$$

In the formulas, s,N,ρ_0 are the zonal wavenumber, buoyancy frequency, and air density, respectively. In particular, $\bar{q}$ (Equation 8) is the zonal-mean quasi-geostrophic potential vorticity, and the subscript φ represents the meridional derivative. All other symbols follow the definitions given above.

3 SNAPSI forecast of the 2019 SH SSW

3.1 A brief review of the 2019 SH SSW

The SH stratospheric polar vortex was already in a weaker-than-normal state during June-August 2019. It is seen from the reanalysis that at the forecast initial time (29 August), the climatological U1060 is around 90 m/s, which is 20 m/s stronger than the speed in 2019 (Fig. 1i). During the 2019 SSW, U1060 experienced three intermittent decreases between 29 August and 18 September, dropping below 20 m/s on 15 September (defined as the SSW onset date). The total deceleration during this period reached about 60 m/s, with a minimum zonal wind of

https://doi.org/10.5194/egusphere-2026-4971
Preprint. Discussion started: 8 September 2026

approximately 10 m/s occurring around 17-18 September. Compared with the major SSW in 2002 (dark gray line in Fig. 1i), the total weakening of U1060 is comparable, but the 2019 event was markedly more gradual, with the 60 m/s reduction occurring over a period of about 21 days, approximately twice as long as in 2002 (11 days) (Fig. 1i). After 18 September 2019, U1060 partially recovered and subsequently fluctuated around 20 m/s for the rest of the forecast period. Based on the characteristics of the 2019 SH SSW and existing reports in literature, the forecast period is divided into three segments: a central period centered on the onset date and the corresponding early and late periods (see caption in Fig. 1a), in order to provide a more comprehensive assessment of the model's performance in forecasting this event.

3.2 Free prediction and biases of the 2019 SH SSW

Figure 1a-f presents the evolution of the U1060 surrounding the 2019 SH SSW in all ensemble members from the free run (gray dashed curves) and the corresponding ensemble means (red curves) for each model. Based on the ensemble mean, at least two models (CNR-ISAC and SNU) failed to forecast this SSW, as their ensemble means do not decrease to below 20 m/s throughout the entire forecast period. In addition, although the UKMO model forecasts the zonal wind at ~20 m/s around 1 October, the SSW onset is delayed by two weeks and occurs at the end of the forecast period. The ensemble mean of ECMWF shows the highest skill of forecasting the SSW, while all other models soon begin to deviate markedly from ERA5 one week after initialization, consistently underestimating the magnitude of westerly weakening. This bias may be related to an underestimation of the upward propagation of waves which will be investigated in the next section.

In addition to a qualitative assessment, we further provide a quantitative evaluation of model forecast performance. The SSW hit ratio is a key probabilistic metric for ensemble forecast evaluation, defined as the fraction of ensemble members that successfully capture the occurrence of an SSW. Only the first instance of U1060 < 20 m/s is counted for each member. This metric can be computed either over the full forecast period or restricted to the central period (Rao et al., 2019; Ayarzagüena et al., 2026). Under a stricter definition, only forecasts that capture the SSW within the central period are considered successful. Hits occurring outside this window, including those during the early and late periods, are classified as false alarms,

https://doi.org/10.5194/egusphere-2026-4971
Preprint. Discussion started: 8 September 2026

indicating forecasts issued at physically implausible times and thus lacking practical predictive value (Taguchi, 2016). Fig. 1g shows the hit ratios for each model across different periods. ECMWF, KMA, and Meteo-France exhibit substantially higher SSW hit ratios than the other models, reaching approximately 40%, with ECMWF achieving the highest value, close to 50%. In contrast, the hit rate of SNU is below 10%, while CNR-ISAC fails to capture any SSW events. In terms of the false alarm ratio, the three models with higher SSW hit ratios also exhibit higher false alarm ratios, generally exceeding 50%. The sum of the SSW hit ratio and the false alarm ratio is close to 100%, indicating that nearly all ensemble members eventually experience a substantial weakening of zonal-mean zonal winds in those models. Furthermore, among the false alarms, only a few members from ECMWF and UKMO issue earlier alarms during the early period, while all models generally tend to predict later alarms during the late period. For the three lower skill models, CNR-ISAC nearly misses SSW events, while SNU and UKMO forecast SSWs too late rather than lacking the ability to capture SSWs.

The ensemble-mean model biases are mainly concentrated in the central period for most models except Meteo-France, which show a bias peak in the late period (Fig. 1h). For the higher-performing models (ECMWF, KMA, and Météo-France), the relatively high SSW hit ratios are associated with a combination of low ensemble-mean biases and small ensemble spreads. Comparing biases among models during the later period, ECMWF and Meteo-France exhibit negative values, indicating an overly stronger deceleration of the westerly winds. In ECMWF, the ensemble spread during the late period exceeds the mean bias amplitude, which is only weakly too slow compared to reanalysis for the remainder of the forecast (Fig. 1b). In contrast, Meteo-France exhibits the largest negative bias during the later period among all models, which is also the largest bias among the three forecast periods. The ensemble spread in Meteo-France is generally smaller than the mean bias magnitude, implying that the model systematically fails to simulate the westerly recovery and tends to forecast a premature breakdown of the polar vortex.

https://doi.org/10.5194/egusphere-2026-4971
Preprint. Discussion started: 8 September 2026

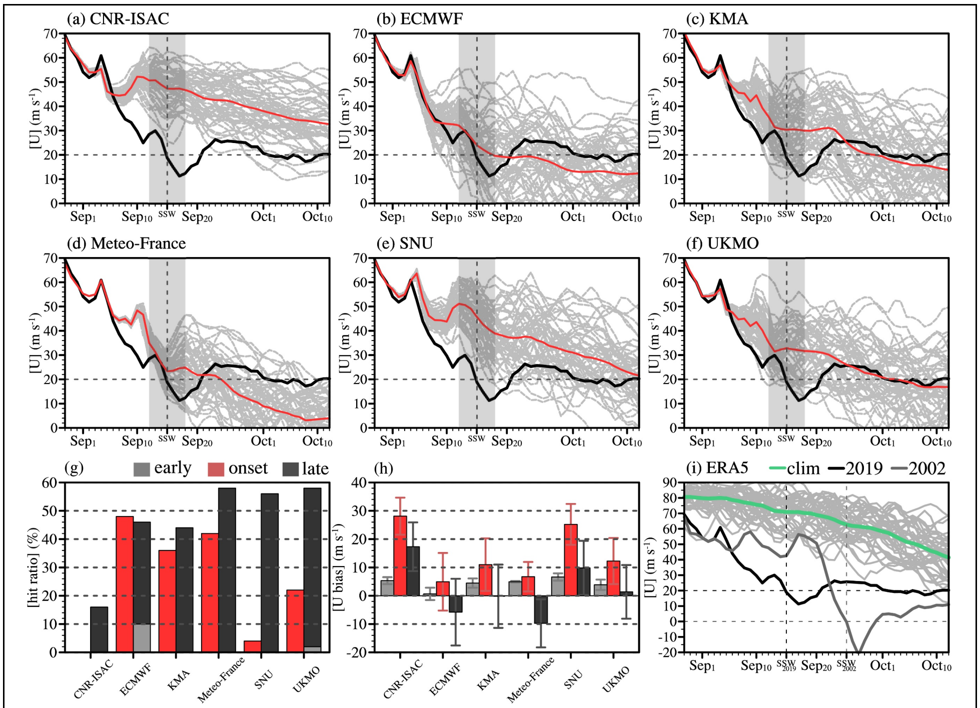

Figure 1. (a-f) Forecasts of U1060 in free runs for six SNAPSI models with ERA5 shown in the black curve. The gray curves are all members, and the red curve is the ensemble mean. The horizontal and vertical dashed lines denote the 20 m/s value and the SSW onset date, respectively. The SSW central period is shaded in gray (12-18 September), while the preceding and subsequent forecast days are defined as the earlier (29 August-11 September) and later (19 September-12 October) periods, respectively. **(g)** SSW hit ratios during three periods in the free runs. An SSW hit refers to an ensemble member predicting U1060 below 20 m/s in the given period. The hit ratios in the central period (±3 days; real hit) are shown in red bars, whereas those in earlier and later periods (false alarms) are displayed in light and dark bars, respectively. **(h)** Ensemble mean biases of U1060 during three periods in the free runs. Error bars indicate one inter-member standard deviation (i.e., ensemble spread). **(i)** Observed U1060 evolutions from September-October during 1979-2019, displayed in light gray curves. The climatology is shown in green. The 2002 and 2019 SH SSW events are highlighted in dark gray and black, respectively.

https://doi.org/10.5194/egusphere-2026-4971
Preprint. Discussion started: 8 September 2026

4 Forecast of the dynamical processes and the role of the stratospheric state

4.1 Tropospheric forcing and wave propagation biases in free experiments

Previous studies have suggested that the occurrence of the 2019 SSW was mainly driven by enhanced tropospheric WN1 forcing. Therefore, we examine how biases in the representation of wave activity evolution are associated with the forecast biases of this SSW. Fig. 2a–f shows the biases of each free experiment relative to ERA5, while Fig. 2g presents the vertical–temporal evolution of the WN1 Eliassen-Palm flux (EPF) vertical component and the 60°S zonal-mean zonal wind in ERA5. Fig. 2h also shows the temporal evolution of the 500 hPa favorable pattern intensity in observations and free runs, representing the tropospheric wave forcing. The temporal evolution of the ensemble correlation coefficients between the favorable pattern intensity and the 100 hPa eddy heat flux three days later in each model are also shown in Fig. 2i, which characterizes the response of the lower stratospheric upward wave flux to tropospheric wave forcing.

Reanalysis shows that the strongest tropospheric wave activity occurred during the early period (29 August–11 September) (Fig. 2g), which generally coincides with the peak intensity of the 500 hPa favorable pattern (Fig. 2h). During this period, the strong upward propagating wave activity extended from the troposphere to ~100 hPa and further into the upper stratosphere. Around the SSW onset (central period, 12–18 September), the upper stratospheric westerlies weakened and reversed to easterlies. Meanwhile, wave dissipation mainly occurred in the middle stratosphere (as shown later in Fig. 3g). After this period, the 500 hPa favorable pattern was no longer maintained and temporarily disappeared (Fig. 2h). Although some intermittent upward wave propagation still occurred in the troposphere, its magnitude was much weaker than the peak during the early period.

SNAPSI models can generally reproduce the intensity of the 500 hPa favorable pattern in the early and central periods (except for CNR-ISAC and SNU). During the late period (after 19 September), the observed favorable pattern temporarily reversed. However, the simulated favorable pattern intensity in the models generally disappeared (i.e., the amplitude became near-zero), indicating that the models struggled to reproduce the observed temporal evolution of the tropospheric forcing after the SSW event. Throughout the forecast period, the 100 hPa

https://doi.org/10.5194/egusphere-2026-4971
Preprint. Discussion started: 8 September 2026

eddy heat flux showed strong consistency with the 500 hPa wave forcing, with correlation coefficients >0.5. This relationship was maximum during the central period, with correlations ~0.8, and there is little spread across models, showing that all models show large sensitivity of the lower stratospheric upward wave flux to tropospheric wave forcing during this event.

The vertical–temporal evolution of vertical wave activity biases in models can be divided into the same three periods. During the early period, all models exhibited too-weak upward wave propagation throughout the stratosphere, probably due to their too-weak favorable pattern (Fig. 2h). Among them, CNR-ISAC and SNU showed the largest biases, consistent with their stronger zonal wind biases, as the westerly biases in the models are often associated with too-weak upward EPF biases. During the late period, the observed EPF experienced a short-term reversal in its upward propagation. Models failed to capture this reversal of favorable pattern (Fig. 2h), resulting in too-strong upward EP flux biases during this period. Subsequently, as the observed favorable pattern recovered in the late period, the pattern intensity in models already disappeared, leading again to too-weak upward propagation biases.

During the early and late periods, the evolution of wave activity in models are roughly consistent between lower and upper levels. Specifically, weakened (enhanced) lower stratospheric wave forcing was generally accompanied by weakened (enhanced) upward wave propagation in the upper stratosphere. However, during the central period, the distribution of wave activity biases exhibited a different structure: weakened upward propagation biases near the tropopause coexisted with enhanced upward propagation biases in the upper stratosphere. As the models that best simulated the SSW evolution, ECMWF, KMA, and Meteo-France simulated a brief enhancement of the favorable pattern around 10 September, but the magnitude of this enhanced wave forcing was too small and the duration was too short. The associated strong upward propagation occurs mainly during 12–14 September in these models, which cannot fully explain the persistent strong upward EPF biases in the upper stratosphere throughout the central period. Moreover, although CNR-ISAC and SNU forecast consistently too-weak wave activity before the central period in the lower stratosphere, they still produce strong upward EPF biases in the upper stratosphere during the central period.

This evidence suggests that the development of too-strong upper stratospheric EPF biases

https://doi.org/10.5194/egusphere-2026-4971
Preprint. Discussion started: 8 September 2026

during the central period was not solely related to tropospheric wave forcing; instead, the stratospheric background state also played an important role in regulating upper stratospheric wave propagation. We explore this possibility in the next section.

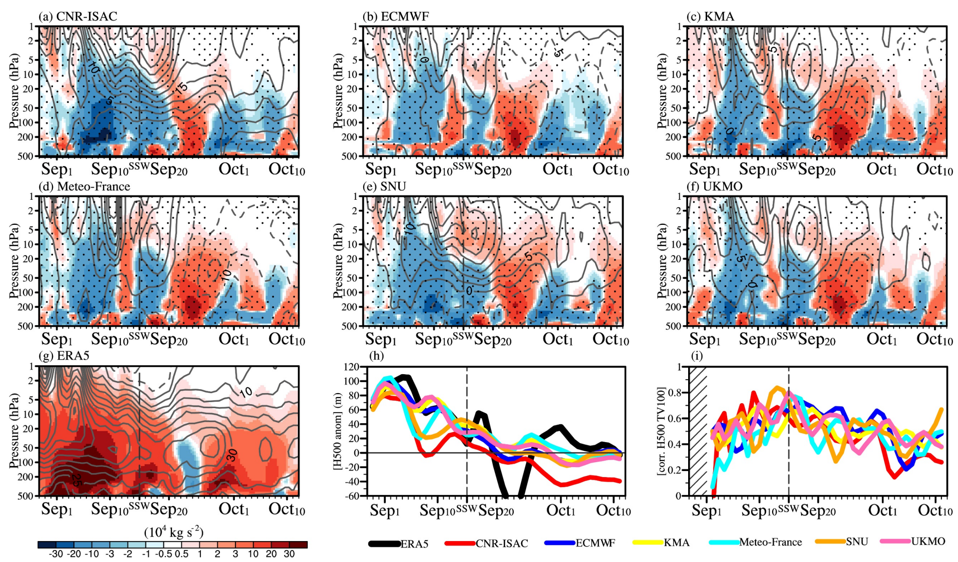

Figure 2. (a-f) Forecast biases of vertical component of wavenumber 1 (WN1) EPF (shading) averaged over 45°S–75°S and zonal mean zonal wind at 60°S (contour; interval 5 m/s) in free runs. Dots show biases at the 95% confidence level according to the *t*-test. **(g)** Observed vertical component of WN1 EPF (shading; the positive value means upward wave propagation) and zonal mean zonal wind at 60°S (contour; interval 5 m/s) in ERA5. **(h)** Strength of 500 hPa favorable pattern (absolute anomalies averaged within the red and blue boxes in Fig. 4) in ERA5 and free runs. **(i)** Inter-ensemble correlations between 500 hPa favorable pattern strength and 3-day lagged 100hPa eddy heat flux averaged over 45°S–75°S in free runs.

4.2 Stratospheric control on wave propagation during the SSW

To better illustrate how the stratospheric state affects the propagation of planetary waves in the upper stratosphere, we compare the early period (Fig. 3a–d) and central period (Fig. 3e–h). The EP flux and the zonal wind in ERA5 and the biases of the corresponding free multi-model mean (MMM) are shown in the left column of Fig. 3, which are used to investigate the

https://doi.org/10.5194/egusphere-2026-4971
Preprint. Discussion started: 8 September 2026

role of wave breaking in decelerating the zonal wind and to evaluate model performance. The observed refractive index (RI) and the RI from the free MMM are presented in the right column, which are used to examine how the background mean flow regulates wave propagation.

During the early period (Fig. 3a–d), low-latitude middle stratospheric easterly winds extended poleward (Fig. 3c). As a result, the dynamical barrier, represented by the critical line (0 m/s), remained around 45°S. Therefore, the EPF convergence region was mainly concentrated in the middle-to-upper stratosphere poleward of 45°S. During the same period, the models exhibited weaker EPF convergence in the middle-to-upper stratosphere (Fig. 3a). Origin of this bias can be primarily attributed to insufficient tropospheric wave forcing, since the horizontal wave propagation is relatively weak in the middle-to-upper stratosphere (see Fig. S1 in the Supplement).

During the central period (Fig. 3e–h), the tropospheric wave forcing had already weakened substantially (Fig. 2h; Fig. 3g), but enhanced waves continued to propagate upward in ERA5. The polar vortex reached its weakest state (Fig. 2g), and the jet core shifted downward to the region between 20–50 hPa (Fig. 3g). Consequently, the critical line continued to move poleward and temporarily arrived at 70°S near the stratopause. Meanwhile, almost the entire midlatitude stratosphere was occupied by negative RI values (Fig. 3h). Such a background state became unfavorable for wave propagation into the upper stratosphere, causing the center of EPF convergence at polar latitudes to shift downward into the middle stratosphere.

In contrast, in models, persistent too weak tropospheric wave forcing resulted in insufficient weakening of the polar jet (Fig. 3e). Therefore, the simulated jet core showed little downward displacement during the central period and remained near 10–20 hPa. This prevented the critical line from extending further poleward, with its maximum poleward extent reaching only ~ 50°S at the stratopause. Consequently, although the EPF entering the stratosphere was consistently weaker than in ERA5, the models still maintained relatively strong upward wave propagation into the upper stratosphere. This explains the strong EPF convergence biases near the stratopause and the weak convergence biases in the middle stratosphere in the MMM. The shift of the observed EPF convergence center between these

https://doi.org/10.5194/egusphere-2026-4971
Preprint. Discussion started: 8 September 2026

two periods, together with the corresponding changes in model biases, demonstrates the stratospheric control on upper-level wave activity.

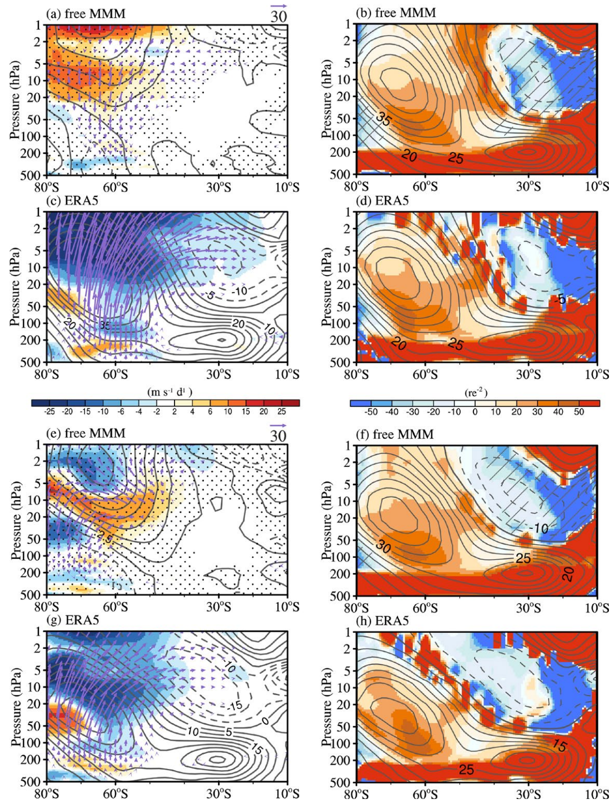

Figure 3. (a) Multi-model multi-ensemble mean (MMM) biases of WN1 EPF (vector), EPF divergence (shading), and zonal mean zonal wind (contour; interval 2.5 m/s) in free runs during the early period (29 August–11 September). Dots show difference at the 95% confidence level, based on the t-test. **(b)** MMM of WN1 refractive index (RI) (shading) and zonal mean zonal wind (contour; interval 5 m/s) in free runs during the early period (29 August-11 September). The hatched shading indicates the negative sign consistency of ensemble members over 90%. **(c)** Observed WN1 EPF, EPF divergence (shading), and zonal mean zonal wind (contour; interval 5 m/s) in ERA5 during the early period. **(d)** Observed WN1 RI (shading), and zonal mean zonal wind (contour; interval 5 m/s) in ERA5 during the early period. **(e-h)** as in **(a-d)**, but for the central period (12–18 September).

https://doi.org/10.5194/egusphere-2026-4971
Preprint. Discussion started: 8 September 2026

4.3 Stratospheric influence on the tropospheric favorable pattern

The previous sections have systematically examined the statistical and dynamical characteristics of model forecast biases during this SSW event and identified the mechanisms responsible for wave activity biases during different periods. In particular, it is emphasized that the stratospheric background state can regulate upper stratospheric wave propagation. Here, we further ask whether changes in the stratospheric state can also influence the tropospheric favorable pattern and the subsequent upward wave propagation. To address this question, we use the SNAPSI nudged and control experiments, in which the stratospheric zonal wind and temperature above 90 hPa are constrained toward the observed and climatological states, respectively. The difference between these two experiments is therefore used to isolate the influence of the weakened stratospheric state. Figure 4a shows the vertical–temporal evolution of the difference in the vertical component of WN1 EPF. Figure 4c–d presents the weekly evolution of the 500 hPa geopotential height differences, while Fig. 4f–h shows the corresponding ERA5 500 hPa geopotential height anomalies for comparison.

ERA5 shows that the 500 hPa favorable pattern persisted from the beginning of the forecast period until the end of the central period (Fig. 4f–h). This pattern consisted of a positive geopotential height anomaly west of the Antarctic Peninsula and a negative anomaly over the southern Indian Ocean, superimposed on the climatological WN1 pattern, and this favorable pattern was also reasonably reproduced in the control runs (Fig. 4c–e, contour). Small differences in the nudged minus control geopotential height anomalies during the first forecast week (29 August–4 September; Fig. 4c, shading) indicate that the stratospheric influence was weak and slightly unfavorable for the development of the favorable pattern. In the following two weeks, however, as the polar vortex continued weakening, the positive anomaly west of the Antarctic Peninsula gradually intensified, while the negative anomaly over the southern Indian Ocean also strengthened but shifted away from the climatological trough.

Overall, during the first forecast week, there were enhanced upward EPF above 90 hPa in nudged minus control runs (Fig. 4a), but this enhancement was not linked with the tropospheric wave forcing. The favorable wave pattern did intensify with the weakening of the polar vortex. However, this enhancement occurred only after the first forecast week, and the magnitude of

https://doi.org/10.5194/egusphere-2026-4971
Preprint. Discussion started: 8 September 2026

the pattern intensification induced by the polar vortex weakening was relatively small, accounting for only 10–20% of the observed amplitude. The EPF differences below 90 hPa (Fig. 4a) also show enhanced upward wave propagation after the first forecast week, consistent with the changes in the tropospheric favorable pattern, which supports the arguments presented in Section 4.3. However, because the stratosphere above 90 hPa was directly constrained in the nudged and control experiments, the EPF differences in this region do not represent the response of the zonal wind to wave activity. Instead, they reflect how wave propagation adjusts to the prescribed background state. Thus, under the weakened prescribed stratospheric state, upward wave propagation above 90 hPa was suppressed in the nudged runs, reflecting the adjustment of wave propagation to the modified mean flow.

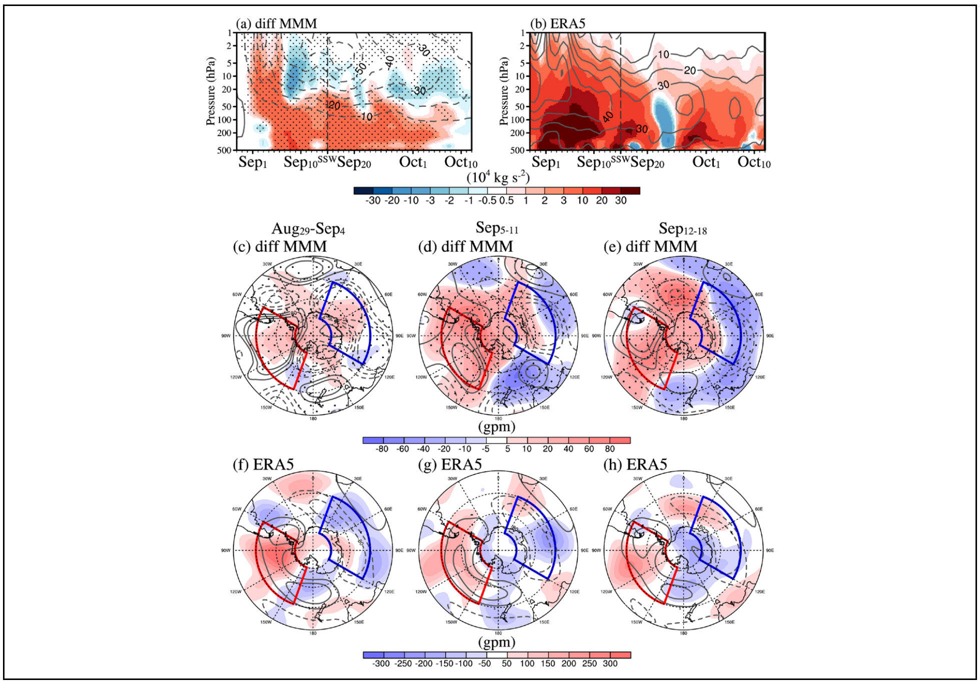

https://doi.org/10.5194/egusphere-2026-4971
Preprint. Discussion started: 8 September 2026

Figure 4. (a) MMM difference of vertical component of WN1 EPF (shading) and zonal mean zonal wind at 60°S (contour; interval 10 m/s) between nudged and control runs. Dots show difference at the 95% confidence level, based on the t-test. **(b)** same as Fig. 2g, shown here for reference. **(c-e)** MMM differences of 500 hPa geopotential height (shading) between nudged and control runs and MMM eddy geopotential height field in control runs (contour; interval: 40 gpm) during three forecast periods. Dots show difference at the 95% confidence level, based on the *t*-test. **(f-h)** Observed 500 hPa geopotential height anomalies (shading) and climatological eddy geopotential height field (contour; interval: 40 gpm) in ERA5 during the same periods. The red and blue boxes indicate the regions used to define the favorable pattern (ridge, 45°S–75°S, 60°W–160°W; and trough, 45°S–75°S, 20°E–120°E).

5 Impact of the 2019 SH SSW event on surface forecasts

5.1 Downward propagation of zonally asymmetric stratospheric signals

Shortly after SSW onset, U1060 experienced a modest recovery to around 25 m/s, but then dropped to below 20 m/s again on 3 October (Fig. 1i). The weak westerly winds are far below the climatological state, indicating a sustained weakening of the stratospheric polar vortex and the early onset of the stratospheric final warming. Existing studies have used the Southern Annular Mode (SAM) to determine whether stratospheric disturbances propagate downward (Rao et al. 2020b; Lim et al. 2021; Feng et al. 2025). The downward impact of the 2019 SH SSW has been estimated to occur around 18 October, far beyond the forecast period considered in this study (29 August–12 October) (Feng et al. 2025). However, using three-dimensional wave activity flux (WAF) diagnostics, we have already identified evidence of a downward-propagating signal with clear zonal asymmetry since 3 October.

Figure 5 shows wave activity flux (WAF) for WN 1-3 and eddy geopotential height averaged over 45°S–75°S for different time periods. From the initial time to 2 October (Fig. 5a), the tropospheric wave source exhibits a relatively symmetric WN1 structure, and a coherent upward-propagating pathway above 500 hPa is mainly confined to 60°W–180°W, where an anomalous high develops over the Antarctic Peninsula. This is consistent with

https://doi.org/10.5194/egusphere-2026-4971
Preprint. Discussion started: 8 September 2026

previous studies highlighting the importance of the Antarctic Peninsula high in enhancing upward eddy heat flux (e.g., Rea et al., 2024). From the lower troposphere to the middle stratosphere, the height ridge and trough show a clear westward tilt with height, indicating a canonical upward-propagating Rossby wave structure.

After 3 October (Fig. 5b), upward wave activity persists over the Western Hemisphere troposphere, while downward-propagating waves appear in the lower stratosphere over the southern Atlantic Ocean when the weakened polar low extends downward. At the end of the forecast period (Fig. 5c–d), the Antarctic Peninsula tropospheric high gradually weakens, and its associated upward wave activity is further reduced. Meanwhile, as stratospheric westerlies continue to weaken, most upward-propagating planetary waves are refracted near the tropopause. The refracted waves converge in the 0°–60°W sector (southern Atlantic Ocean), where it merges with wave flux descending from the stratosphere, forming a coherent downward-propagating wave activity. This process leads to an eastward-tilted vertical structure of troughs extending into the lower troposphere, consistent with the typical Rossby wave downward propagation or refraction process (Kodera et al., 2008). These results imply that a zonally asymmetric downward-propagating wave process already emerges during 3–12 October, but it remains weak and is strongly confined to the southern Atlantic Ocean sector.

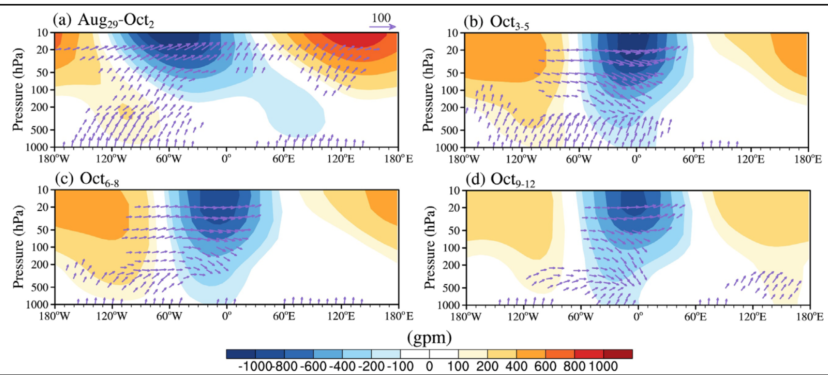

Figure 5. (a) Observed WAF (vector; units: m^2/s^2) by WN 1-3 and eddy potential height (shading; units: gpm) averaged within 45°S-75°S from 29 August to 2 October from ERA5. **(b-c)** As in (a), but for the time evolutions during the rest of three forecast periods (3-12 October).

https://doi.org/10.5194/egusphere-2026-4971
Preprint. Discussion started: 8 September 2026

5.2 Stratospheric role to the tropospheric forecast

Figure 6g shows the observed 500 hPa geopotential height anomalies (major plot; shading), the climatological ridges and troughs (major plot; contours) and the vertical component of the 100 hPa WAF (minor plot) averaged during 3–12 October. The corresponding nudged minus control differences, representing the isolated impact of stratospheric perturbations, are also shown in Fig. 6a-f. Two climatological ridges are located over southern Africa and southern South America in ERA5, respectively, with the latter being stronger, reaching a maximum of about 90 gpm and extending westward to the west of New Zealand (Fig. 6g). Pronounced downward wave activity is observed in the lower stratosphere over 0°–60°W, while upward wave activity appears over 120°W–180°W (see also Fig. 5). These correspond respectively to an anomalous low in the Atlantic sector and an anomalous high in the Pacific sector. Both anomaly centers are superimposed near the climatological ridge over southern South America. In midlatitudes, high anomalies are also present over southern Africa, Australia, and central South America. The highs over southern Africa and central South America are likewise superimposed near the corresponding climatological ridges.

In the control experiments (Fig. 6a–f, contours), CNR-ISAC forecasts a markedly different eddy geopotential height pattern from other models, characterized by an overly strong high extending from southern South America westward and equatorward. This high contains three distinct centers located over southern South America, the subtropical South Pacific, and southern Australia, respectively. In addition, the southern Africa high is substantially weaker than its observed climatology. In contrast, the remaining five models reasonably reproduce the observed double-ridge structure and its overall amplitude. SNU shows a northward-biased and overestimated southern South American ridge with an elusive minor center exceeding 50 gpm. Three models (ECMWF, KMA, and Meteo-France) forecast a too strong high (~10 gpm) over Australia in the control runs.

In the nudged minus control differences, models consistently produce a negative SAM-like response, characterized by positive geopotential height anomalies over the Antarctic and negative anomalies in the SH midlatitudes. This phenomenon is consistent with previous studies, which have shown that stratospheric signals emerge earlier at high latitudes and exhibit

https://doi.org/10.5194/egusphere-2026-4971
Preprint. Discussion started: 8 September 2026

a more zonally symmetric structure over Antarctica (e.g., Garfinkel et al., 2023). The vertical component of the 100 hPa wave activity flux indicates that the stratospheric wave perturbations are forecast farther westward by approximately 60° longitude relative to observations with an underestimated amplitude. The corresponding geopotential height response shows a low anomaly center over 45°S–75°S, 60°W–120°W and a high anomaly center over 60°S–75°S, 0°–120°E. Five of the six models except CNR-ISAC forecast the low anomalies over 60°W–120°W, nearly collocated with the ridge over southern South America in the control runs. This suggests that stratospheric perturbations primarily act to weaken this ridge in the nudged runs, and the westward strengthening of the ridge is relatively weaker than observed. Over Australia, these five models capture a meridional dipole structure characterized by a trough to the south and a ridge to the north. This pattern has been linked to reduced precipitation over eastern Australia during late October (Gibson et al., 2017; Henderson et al., 2024). Models with the stratospheric contribution forecast this dipole pattern too early before it appears in the observations, and this may also be associated with the overestimation of the downward coupling by S2S models (Garfinkel et al. 2025).

https://doi.org/10.5194/egusphere-2026-4971
Preprint. Discussion started: 8 September 2026

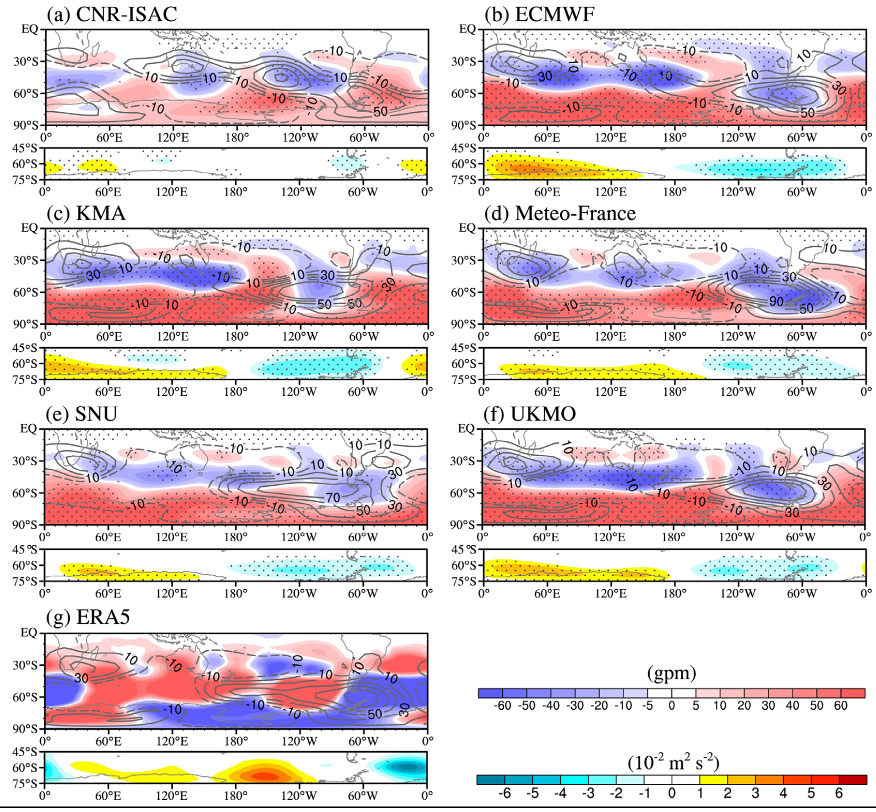

Figure 6. (a-f) Difference of 500 hPa geopotential height (major plot; shading) and vertical component of WN1-3 WAF (minor plot; shading) at 100 hPa between nudged and control runs during 3-12 October. Dots show difference at the 95% confidence level based on the t-test. The 500 hPa eddy geopotential height in the control runs (major plot; contour; interval 20 gpm) are highlighted in red (positive) and blue (negative), respectively. **(g)** ERA5 500 hPa geopotential height anomalies (major plot; shading) and vertical component of WN1-3 WAF (minor plot; shading) at 100 hPa during 3-12 October. The climatological ridges and troughs at 500 hPa are in solid (positive) and dashed (negative) contours, respectively.

5.3 Forecast skill of precipitation attributed to the stratospheric signals

Figure 7 shows observed precipitation anomalies and the nudged minus control run differences for the SNAPSI models. Two focused regions are highlighted in orange boxes, eastern Australia (EA) and South America (SA). Both EA and SA witnessed negative

https://doi.org/10.5194/egusphere-2026-4971
Preprint. Discussion started: 8 September 2026

precipitation anomalies after the SSW onset (Fig.7g). In EA, the mean rainfall anomaly is approximately −0.3 mm/day, with maximum anomaly center near Brisbane, approaching −1 mm/day. In SA, the drought is more widespread and more intense, with the anomaly magnitude exceeding 1 mm/day in most of the region and reaching 1.5 mm/day in some spots. Such drought conditions are closely linked to the circulation patterns (Fig. 6g). Although a weak low pressure anomaly center appears over eastern EA, most of EA is predominantly controlled by a broad high pressure circulation, which suppresses precipitation. In central SA, an anomalous high disrupts the Amazon moisture inflow pathway. Over southern SA, an anomalous high enhances the climatological ridge to the west of SA, while the downward-propagating stratospheric low weakens the eastern flank of the climatological ridge; this dipole establishes a meridional flow corridor that allows dry air to move inland from high latitudes.

Out of SNAPSI models, three (ECMWF, KMA, and UKMO) simulate evident negative precipitation contributions from the stratosphere over EA. These three models show higher skill of forecasting the EA northern ridge – southern trough dipole under nudged conditions, which is reported favorable for EA's drought conditions in late spring (Feng et al., 2025), although this pattern was not yet clearly established in ERA5 during early October. These models also exhibit better consistency for the stratospheric forcing, tropospheric circulation anomaly structure, and rainfall response. Two models (SNU and UKMO) forecast significant but limited negative precipitation anomalies over SA. This can be possibly attributed to two factors: On one hand, the downward-propagating low anomaly center is forecast too westward (Fig. 6a–f), leading to excessive weakening of the southern SA ridge. On the other hand, most models (except SNU and UKMO) fail to capture the enhanced high anomaly center over central SA.

Southern Africa also experienced severe drought (Fig. 7g), but models do not provide evidence that stratospheric perturbations can reduce rainfall over Southern Africa by driving tropospheric circulation variations (Fig. 6). It might imply that the drought over Southern Africa might be forced by other factors at such a short lag relative to the SSW onset.

https://doi.org/10.5194/egusphere-2026-4971
Preprint. Discussion started: 8 September 2026

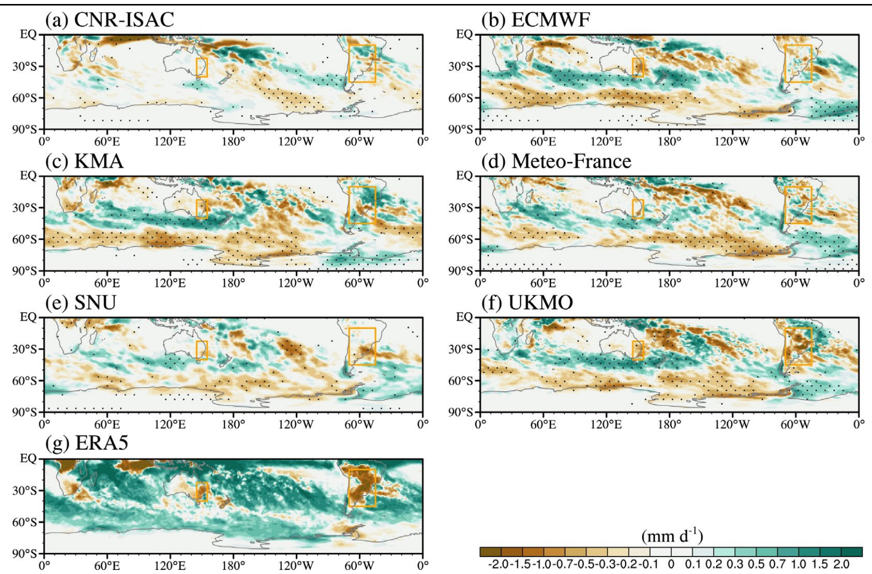

Figure 7. As in Fig. 6, but for total precipitation differences between the nudged and control runs. The focused regions, eastern Australia (EA; 22.5°S-40°S, 145°E-155°E) and South America (SA; 10°S-45°S, 45°W-70°W), are highlighted in the orange boxes.

Based on 50 ensemble members, the distribution of forecast precipitation anomalies in the EA and SA regions are analyzed for each run and each model (Fig. 8). In EA (Fig. 8a), four of the six models (except ECMWF and UKMO) overestimate the observed negative precipitation anomaly in the control run ensemble means. Specifically, the observed precipitation anomaly is −0.3 mm/day, while the control runs from CNR-ISAC, KMA, Meteo-France, and SNU forecast too large negative anomalies, with the magnitude of 4.3, 1.7, 2.0, and 3.7 times the observed value (1.3/0.3, 0.5/0.3, 0.6/0.3, and 1.1/0.3), respectively. This indicates that models tend to overestimate the contribution of boundary forcing (e.g., oceanic conditions) to the EA precipitation deficit without the stratospheric signal interference. In particular, CNR-ISAC forecasts an unrealistically strong anticyclonic ridge over EA in the control run (Fig. 6a). This partly explains why the nudged experiments in these four models do not show a stronger drying response over EA. In contrast, ECMWF and UKMO with dry anomalies close to observed over EA in the control runs exhibit the strongest additional drying signals in the nudged runs. Overall, the ensemble distribution shows that the EA precipitation consistently shifts toward lower

https://doi.org/10.5194/egusphere-2026-4971
Preprint. Discussion started: 8 September 2026

values in the nudged runs. This indicates a consistent tendency toward EA drier anomalies when the stratospheric signals are more realistic.

Models exhibit large spread of forecast rainfall over SA. CNR-ISAC, ECMWF, and Meteo-France fail to reproduce negative rainfall anomalies in the control run ensemble mean, and stratospheric perturbations do not lead to additional dring. This indicates that lower-boundary forcing alone does not ensure realistic forecast of SA rainfall anomalies in these models, and that the SA rainfall is also insensitive to stratospheric perturbations. KMA and UKMO show positive precipitation anomalies in all three experiments, with lower quartiles still remaining above the climatological mean. The unrealistic wet anomalies are consistent with the enhanced low centered over western SA and the northward extension of the southern SA ridge in the control runs (Fig. 6c, f). In contrast, SNU exhibits consistently negative precipitation anomalies across nearly all ensemble members, indicating a severe dry bias. This is closely linked to an overly strong and broad southern SA ridge in the control experiment (Fig. 6e), suppressing precipitation over SA. In short, the contribution of the stratospheric perturbation signal to precipitation over SA is neither as model-consistent nor as strong as that over EA.

https://doi.org/10.5194/egusphere-2026-4971
Preprint. Discussion started: 8 September 2026

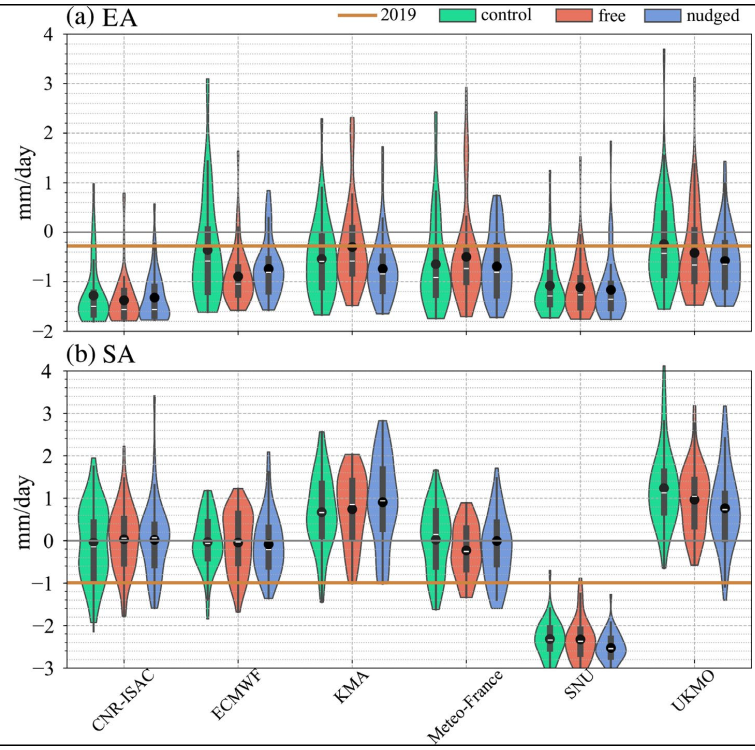

Figure 8. Violin plots (outer) and box-and-whisker plots (inner) of forecast total precipitation anomalies relative to the ERA5 climatology (units: mm/day) in **(a)** EA and **(b)** SA, for control (green), free (red), nudged (blue) runs during 3-12 October. The ensemble mean is shown in black dot. The upper quartile, lower quartile, and median are shown in box's top, bottom, and white dash, respectively. The width of the violin plot indicates the distribution density. The observed precipitation is shown in the horizontal brown reference line..

6 Summary and discussion

This study examines planetary wave activity during a rare SH SSW event and the short-term near-surface weather response to stratospheric nudging in SNAPSI models. Under the framework of SNAPSI, two stratospheric nudged experiments are examined to assess the role of a well resolved stratospheric state in forecasting the SSW event and isolating its contribution to subseasonal weather forecasts.

https://doi.org/10.5194/egusphere-2026-4971
Preprint. Discussion started: 8 September 2026

Using outputs for an initialization before the SSW onset, the model performance of forecasting the U1060 evolution and the primary biases is evaluated. The high SSW hit ratios in high-skill models (ECMWF, KMA, and Meteo-France) show a smaller ensemble mean bias but a larger ensemble spread during the SSW onset. Larger ensemble spreads accompanying higher hit ratios in those models also tends to give larger false alarm ratios. CNR-ISAC exhibits little skill of forecasting SSW events and even fails to capture any SSW onset. In contrast, the forecast errors in SNU and UKMO are primarily due to the delayed onset timing of the SSW. Meteo-France successfully reproduces the SSW hit ratio and the associated wind deceleration during the central period, but it shows little skill in forecasting the later recovery of westerlies. This may lead to a premature breakdown of the polar vortex in the model. This finding is consistent with Lawrence et al. (2022), which finds that Meteo-France initialized in early spring tends to forecast a too early stratospheric final warming at the end of the forecast period.

The SH SSW was primarily driven by persistent tropospheric WN1 forcing associated with the development of an anomalous high over the Antarctic Peninsula (e.g., Shen et al., 2020; Rao et al. 2020; Ayarzagüena et al., 2026). The evolution of planetary wave activity during the SSW was determined in large part, but not fully, by tropospheric forcing. During the early and late periods, model biases in upward wave propagation were closely linked to biases in the representation of the tropospheric favorable pattern. In contrast, during the central period, the upper stratospheric wave activity biases could not be explained by tropospheric forcing alone. Rather, the stratospheric background state played an important role in regulating wave propagation and determining the location of EPF convergence through its modulation of the critical line and refractive index structure. Models with insufficient weakening of the polar jet maintained a less favorable background state for wave dissipation in the middle stratosphere, resulting in excessive upward wave propagation into the upper stratosphere. By comparing the nudged and control experiments, this study further shows that a more realistic stratospheric state can also modify the tropospheric favorable pattern, although the magnitude of this influence is relatively small compared with the direct tropospheric forcing. These results highlight that the stratosphere is not only a passive responder to tropospheric wave forcing but also actively regulates planetary wave evolution.

https://doi.org/10.5194/egusphere-2026-4971
Preprint. Discussion started: 8 September 2026

This study also shows downward propagation of zonally asymmetric weakened polar vortex signals over the Atlantic sector in early October. These asymmetric signals precede the observed negative SAM by nearly two weeks, consistent with Feng et al. (2025), highlighting the importance of the zonally asymmetric stratospheric state for surface impacts during the 2019 SH SSW. The pure stratospheric contribution to the subseasonal forecasts is further isolated by comparing the difference between the nudged and control experiments. All six models consistently show that the negative SAM-like signal has already propagated into the troposphere much earlier than the observations, indicating that purely tropospheric processes delayed the observed onset of the negative SAM.

Three models (ECMWF, KMA and UKMO) show significantly drier conditions over eastern Australia (EA) under the nudged stratosphere compared to the climatological stratosphere due to the more realistic forecast of the geopotential height dipole over EA. As a consequence, these three models also better forecast the EA rainfall, consistent with Feng et al. (2025). The remaining three models (CNR-ISAC, Meteo-France and SNU) show a weaker stratospheric signal in EA rainfall, and impacts of the lower-boundary conditions are more dominant in those models. Most models (except SNU) show a wet bias in South America (SA) in the control experiments, primarily due to the enhanced low pressure over western SA. However, it is still difficult to attribute this enhanced low pressure to the lower-boundary conditions or to the absence of stratospheric perturbations. The nudged stratosphere fails to improve the SA rainfall forecasts at such a short lag relative to the SSW onset. The insensitivity of the SA rainfall response to the stratospheric perturbation is associated with the westward-shifted downward WAF, which reflects a westward displacement of the wave propagation pathway and consequently weaken the climatological ridge over southern SA. Models fail to forecast the anomalous high over central SA. It is still a challenge to forecast the correct position of downward WAF and SA precipitation.

It has been widely acknowledged that a resolved stratospheric state plays a crucial role in modulating wave propagation and can improve subseasonal weather forecasts (Dai et al., 2025; Lee et al., 2025). However, it cannot fully account for all biases arising during different forecasts (Huang et al., 2026). In addition, the nudged stratospheric state appears to not be

https://doi.org/10.5194/egusphere-2026-4971
Preprint. Discussion started: 8 September 2026

related to the severe drought over central and southern Africa, suggesting that other processes may play a more dominant role in driving regional weather extremes. Considering that SNAPSI experiments are primarily based on case studies, some conclusions derived from specific event may not be applicable to other cases. Nevertheless, the SNAPSI framework provides an unprecedented opportunity to investigate the formation and impacts of this rare SH extreme event in 2019 (Feng et al. 2025). This unique case provides useful insights into the stratospheric role in shaping subseasonal forecasts and the current capability of stratosphere-resolved forecast systems.

Data Availability

The SNAPSI models outputs used in this study comes from CEDA (https://catalogue.ceda.ac.uk/uuid/0a5a1ce22fb047749e040879efa8e9b5). The ERA5 reanalysis used in this study comes from ECMWF Climate Data Store (https://cds.climate.copernicus.eu/datasets).

Author contributions

J.R., C.I.G., A.H.B., and B.A. provided guidance and supervised the research. K.F. drafted the initial manuscript. All authors contributed to the writing of the manuscript and its revisions.

Competing interests

At least one of the (co-)authors is a member of the editorial board of Weather and Climate Dynamics.

Special issue statement

This article is part of the special issue "Stratospheric impacts on climate variability and predictability in nudging experiments".

https://doi.org/10.5194/egusphere-2026-4971
Preprint. Discussion started: 8 September 2026

Acknowledgments

This work was finished on the JASMIN platform, the UK's collaborative data analysis environment (https://www.jasmin.ac.uk) (Lawrence et al., 2013). We acknowledge CEDA for providing outputs for SNAPSI models with three experiments (free, nudged, and control). We thank ECMWF for providing the ERA5 reanalysis.

Financial support

This work is jointly supported by the National Natural Science Foundation of China (grant nos. 42322503 and 42361144843).

References

Allen, D. R., Bevilacqua, R. M., Nedoluha, G. E., Randall, C. E., and Manney, G. L.: Unusual stratospheric transport and mixing during the 2002 Antarctic winter, Geophys. Res. Lett., 30(12), https://doi.org/10.1029/2003GL017117, 2003.

Ayarzagüena, B., Butler, A. H., Hitchcock, P., Garfinkel, C. I., Lawrence, Z. D., Ning, W., Rupp, P., Wu, Z., Afargan-Gerstman, H., Calvo, N., de la Cámara, A., Jucker, M., Koren, G., De Maeseneire, D., Manney, G. L., Osman, M., Taguchi, M., Barton, C., Hong, D.-C., Hyun, Y.-K., Kim, H., Knight, J., Malguzzi, P., Mastrangelo, D., Oh, J., Polichtchouk, I., Richter, J. H., Simpson, I. R., Son, S.-W., Specq, D., and Stockdale, T.: The role of the stratospheric state in upward wave flux prior to sudden stratospheric warmings: a SNAPSI analysis, Weather Clim. Dynam., 7(1), 411–437, https://doi.org/10.5194/wcd-7-411-2026, 2026.

Baldwin, M. P., Ayarzagüena, B., Birner, T., Butchart, N., Butler, A. H., Charlton-Perez, A. J., Domeisen, D. I. V., Garfinkel, C. I., Garny, H., Gerber, E. P., Hegglin, M. I., Langemetz, U., Pedatella, N. M.: Sudden stratospheric warmings, Rev. Geophys., 59(1), e2020RG000708, https://doi.org/10.1029/2020RG000708, 2021.

Baldwin, M. P., and Dunkerton, T. J.: Stratospheric harbingers of anomalous weather regimes, Science, 294(5542), 581–584, https://doi.org/10.1126/science.1063315, 2001.

Butler, A. H., and Gerber, E. P.: Optimizing the definition of a sudden stratospheric warming,

https://doi.org/10.5194/egusphere-2026-4971
Preprint. Discussion started: 8 September 2026

J. Clim., 31(6), 2337–2344, https://doi.org/10.1175/JCLI-D-17-0648.1, 2018.

Butler, A. H., Seidel, D. J., Hardiman, S. C., Butchart, N., Birner, T., and Match, A.: Defining sudden stratospheric warmings, Bull. Am. Meteorol. Soc., 96(11), 1913–1928, https://doi.org/10.1175/BAMS-D-13-00173.1, 2015.

Cai, W., van Rensch, P., Cowan, T., and Hendon, H. H.: Teleconnection pathways of ENSO and the IOD and the mechanisms for impacts on Australian rainfall, J. Clim., 24(15), 3910–3923, https://doi.org/10.1175/2011JCLI4129.1, 2011.

Charlton, A. J., and Polvani, L. M.: A new look at stratospheric sudden warmings. Part I: climatology and modeling benchmarks, J. Clim., 20(3), 449–469, https://doi.org/10.1175/JCLI3996.1, 2007.

Chwat, D., Garfinkel, C. I., Chen, W., and Rao, J.: Which sudden stratospheric warming events are most predictable?, J. Geophys. Res. Atmos., 127(18), e2022JD037521, https://doi.org/10.1029/2022JD037521, 2022.

Dai, Y., Hitchcock, P., Butler, A. H., Garfinkel, C. I., and Seviour, W. J. M.: Assessing stratospheric contributions to subseasonal predictions of precipitation after the 2018 sudden stratospheric warming from the SNAPSI project, Weather Clim. Dynam., 6(3), 841–862, https://doi.org/10.5194/wcd-6-841-2025, 2025.

ECMWF: IFS documentation cy43r1 – Part V: Ensemble prediction system, ECMWF Technical Documentation, 2016.

Edmon, H. J., Hoskins, B. J., and McIntyre, M. E.: Eliassen-Palm cross sections for the troposphere, J. Atmos. Sci., 37(12), 2600–2616, https://doi.org/10.1175/1520-0469(1980)037<2600:EPCSFT>2.0.CO;2, 1980.

Feng, K., Rao, J., Garfinkel, C. I., Butler, A. H., Jie, W., Wu, T., Hitchcock, P., Lim, E.-P., Dowdy, A. J., and Seviour, W.: Can stratospheric nudging improve surface predictability? Insights from the 2019 Southern Hemisphere sudden stratospheric warming, npj Clim. Atmos. Sci., 8(1), 353, https://doi.org/10.1038/s41612-025-01234-2, 2025.

Garfinkel, C. I., White, I., Gerber, E. P., Son, S.-W., and Jucker, M.: Stationary waves weaken and delay the near-surface response to stratospheric ozone depletion, J. Clim., 36(2), 565-583. https://doi.org/10.1175/JCLI-D-21-0874.1, 2023.

https://doi.org/10.5194/egusphere-2026-4971
Preprint. Discussion started: 8 September 2026

Garfinkel, C. I., et al. : A process-based evaluation of biases in extratropical stratosphere–troposphere coupling in subseasonal forecast systems, Weather Clim. Dynam., 6(1), 171-195. 10.5194/wcd-6-171-2025, 2025.

Gibson, P. B., Pitman, A. J., Lorenz, R., and Perkins-Kirkpatrick, S. E.: The role of circulation and land surface conditions in current and future Australian heat waves, J. Clim., 30(24), 9933–9948, https://doi.org/10.1175/JCLI-D-17-0265.1, 2017.

Henderson, C. R., Reeder, M. J., Parker, T. J., Quinting, J. F., and Jakob, C.: Summer heatwaves in southeastern Australia, Q. J. Roy. Meteorol. Soc., 150(764), 4285–4305, https://doi.org/10.1002/qj.4816, 2024.

Hersbach, H., Bell, B., Berrisford, P., Hirahara, S., Horányi, A., Muñoz-Sabater, J., Nicolas, J., Peubey, C., Radu, R., Schepers, D., Simmons, A., Soci, C., Abdalla, S., Abellan, X., Balsamo, G., Bechtold, P., Biavati, G., Bidlot, J., Bonavita, M., De Chiara, G., Dahlgren, P., Dee, D., Diamantakis, M., Dragani, R., Flemming, J., Forbes, R., Fuentes, M., Geer, A., Haimberger, L., Healy, S., Hogan, R. J., Hólm, E., Janisková, M., Keeley, S., Laloyaux, P., Lopez, P., Lupu, C., Radnoti, G., De Rosnay, P., Rozum, I., Vamborg, F., Villaume, S., and Thépaut, J.-N.: The ERA5 global reanalysis, Q. J. Roy. Meteorol. Soc., 146(730), 1999–2049, https://doi.org/10.1002/qj.3803, 2020.

Hitchcock, P., Butler, A. H., Charlton-Perez, A. J., Garfinkel, C. I., Stockdale, T., Anstey, J., Mitchell, D., Domeisen, D. I. V., Wu, T., Lu, Y., Mastrangelo, D., Malguzzi, P., Lin, H., Muncaster, R., Merryfield, W., Sigmond, M., Xiang, B., Jia, L., Hyun, Y.-K., Oh, J., Specq, D., Simpson, I. R., Richter, J. H., Barton, C., Knight, J., Lim, E.-P., and Hendon, H. H.: Stratospheric Nudging And Predictable Surface Impacts (SNAPSI): a protocol for investigating the role of stratospheric polar vortex disturbances in subseasonal to seasonal forecasts, Geosci. Model Dev., 15(13), 5073–5092, https://doi.org/10.5194/gmd-15-5073-2022, 2022.

Huang, J., Hitchcock, P., Tian, W., Li, Q., and He, L.: Why do extended-range forecasts underpredict the extreme negative Pacific/North American pattern in February 2018?, J. Geophys. Res. Atmos., 131(7), e2025JD045964, https://doi.org/10.1029/2025JD045964, 2026.

https://doi.org/10.5194/egusphere-2026-4971
Preprint. Discussion started: 8 September 2026

Jucker, M., and Goyal, R.: Ozone-forced southern annular mode during Antarctic stratospheric warming events, Geophys. Res. Lett., 49(4), e2021GL095270, https://doi.org/10.1029/2021GL095270, 2022.

Kodera, K., Mukougawa, H., and Itoh, S.: Tropospheric impact of reflected planetary waves from the stratosphere, Geophys. Res. Lett., 35(16), https://doi.org/10.1029/2008GL034575, 2008.

Koo, M.-S., Song, K., Kim, J.-E., Son, S.-W., Chang, E.-C., Jeong, J.-H., Kim, H., Moon, B.-K., Park, R. J., Yeh, S.-W., Yoo, C., and Hong, S.-Y.: The Global/Regional Integrated Model system (GRIMs): an update and seasonal evaluation, Asia-Pac. J. Atmos. Sci., 59(2), 113–132, https://doi.org/10.1007/s13143-022-00297-y, 2023.

Lawrence, B. N., Bennett, V. L., Churchill, J., Juckes, M., Kershaw, P., Pascoe, S., Pepler, S., Pritchard, M., and Stephens, A.: Storing and manipulating environmental big data with JASMIN, Proc. IEEE Big Data Conf., 2013, https://doi.org/10.1109/BigData.2013.6691556, 2013.

Lawrence, Z. D., Abalos, M., Ayarzagüena, B., Barriopedro, D., Butler, A. H., Calvo, N., de la Cámara, A., Charlton-Perez, A. J., Domeisen, D. I. V., Dunn-Sigouin, E., García-Serrano, J., Garfinkel, C. I., Hindley, N. P., Jia, L., Jucker, M., Karpechko, A. Y., Kim, H., Lang, A. L., Lee, S. H., Lin, P., Osman, M., Palmeiro, F. M., Perlwitz, J., Polichtchouk, I., Richter, J. H., Schwartz, C., Son, S.-W., Erner, I., Taguchi, M., Tyrrell, N. L., Wright, C. J., and Wu, R. W.-Y.: Quantifying stratospheric biases and identifying their potential sources in subseasonal forecast systems, Weather Clim. Dynam., 3(3), 977–1001, https://doi.org/10.5194/wcd-3-977-2022, 2022.

Lee, R. W., Charlton-Perez, A. J., and Lee, S. H.: Stratospheric impacts on weather regimes following the 2018 and 2019 sudden stratospheric warmings, Geophys. Res. Lett., 52(15), e2025GL115668, https://doi.org/10.1029/2025GL115668, 2025.

Liguori, G., McGregor, S., Singh, M., Arblaster, J., and Di Lorenzo, E.: Revisiting ENSO and IOD contributions to Australian precipitation, Geophys. Res. Lett., 49(1), e2021GL094295, https://doi.org/10.1029/2021GL094295, 2022.

Lim, E.-P., Hendon, H. H., Boschat, G., Hudson, D., Thompson, D. W. J., Dowdy, A. J., and

https://doi.org/10.5194/egusphere-2026-4971
Preprint. Discussion started: 8 September 2026

Arblaster, J. M.: Australian hot and dry extremes induced by weakenings of the stratospheric polar vortex, Nat. Geosci., 12(11), 896–901, https://doi.org/10.1038/s41561-019-0456-x, 2019.

Lim, E.-P., Hendon, H. H., Butler, A. H., Thompson, D. W. J., Lawrence, Z. D., Scaife, A. A., Shepherd, T. G., Polichtchouk, I., Nakamura, H., Kobayashi, C., Comer, R., Coy, L., Dowdy, A., Garreaud, R. D., Newman, P. A., and Wang, G.: The 2019 Southern Hemisphere stratospheric polar vortex weakening and its impacts, Bull. Am. Meteorol. Soc., 102(6), E1150–E1171, https://doi.org/10.1175/BAMS-D-20-0112.1, 2021.

Liu, G., Hirooka, T., Eguchi, N., and Krüger, K.: Dynamical evolution of a minor sudden stratospheric warming in the Southern Hemisphere in 2019, Atmos. Chem. Phys., 22(5), 3493–3505, https://doi.org/10.5194/acp-22-3493-2022, 2022.

Ma, C., Yang, P., Tan, X., and Bao, M.: Possible causes of the occurrence of a rare Antarctic sudden stratospheric warming in 2019, Atmosphere, 13(1), 147, https://doi.org/10.3390/atmos13010147, 2022.

MacLachlan, C., Arribas, A., Peterson, K. A., Maidens, A., Fereday, D., Scaife, A. A., Gordon, M., Vellinga, M., Williams, A., Comer, R. E., Camp, J., Xavier, P., and Madec, G.: Global seasonal forecast system version 5 (GloSea5): a high-resolution seasonal forecast system, Q. J. Roy. Meteorol. Soc., 141(689), 1072–1084, https://doi.org/10.1002/qj.2396, 2015.

Mastrangelo, D., and Malguzzi, P.: Verification of two years of CNR-ISAC subseasonal forecasts, Weather Forecast., 34(2), 331–344, https://doi.org/10.1175/WAF-D-18-0091.1, 2019.

Newman, P. A., and Nash, E. R.: The unusual Southern Hemisphere stratosphere winter of 2002, J. Atmos. Sci., 62(3), 614–628, https://doi.org/10.1175/JAS-3323.1, 2005.

Noguchi, S., Kuroda, Y., Kodera, K., and Watanabe, S.: Robust enhancement of tropical convective activity by the 2019 Antarctic sudden stratospheric warming, Geophys. Res. Lett., 47(15), e2020GL088743, https://doi.org/10.1029/2020GL088743, 2020.

Plumb, R. A.: On the three-dimensional propagation of stationary waves, J. Atmos. Sci., 42(3), 217–229, https://doi.org/10.1175/1520-0469(1985)042<0217:OTTDPO>2.0.CO;2, 1985.

Purich, A., Arblaster, J. M., Boschat, G., Gillett, Z. E., Hobbs, W., Jucker, M., Lim, E.-P., Udy,

https://doi.org/10.5194/egusphere-2026-4971
Preprint. Discussion started: 8 September 2026

D., Abram, N., Campitelli, E., Doddridge, E., England, M. H., King, A., Menviel, L., Meyer, A., Ortiz Guzmán, V., Roy, R., Rudeva, I., Spence, P., Strutton, P. G., and Ziehn, T.: Southern annular mode dynamics, projections and impacts in a changing climate, Nat. Rev. Earth Environ., 7(1), 24–42, https://doi.org/10.1038/s43017-025-00746-y, 2026.

Rao, J., Garfinkel, C. I., Chen, H., and White, I. P.: The 2019 New Year stratospheric sudden warming and its real-time predictions in multiple S2S models, J. Geophys. Res. Atmos., 124(21), 11155–11174, https://doi.org/10.1029/2019JD030826, 2019.

Rao, J., Garfinkel, C. I., and White, I. P.: Predicting the downward and surface influence of the February 2018 and January 2019 sudden stratospheric warming events in S2S models, J. Geophys. Res. Atmos., 125(2), e2019JD031919, https://doi.org/10.1029/2019JD031919, 2020a.

Rao, J., Garfinkel, C. I., White, I. P., and Schwartz, C.: The Southern Hemisphere minor sudden stratospheric warming in September 2019 and its predictions in S2S models, J. Geophys. Res. Atmos., 125(14), e2020JD032723, https://doi.org/10.1029/2020JD032723, 2020b.

Rao, J., Garfinkel, C. I., Zhang, X., and Lu, Q.: Subseasonal to seasonal prediction of continental cold following the sudden stratospheric warming in the 2022/23 winter, Clim. Dyn., 63(1), 75, https://doi.org/10.1007/s00382-024-07582-8, 2025.

Rea, D., Elsbury, D., Butler, A. H., Sun, L., Peings, Y., and Magnusdottir, G.: Interannual influence of Antarctic sea ice on Southern Hemisphere stratosphere-troposphere coupling, Geophys. Res. Lett., 51(15), e2023GL107478. https://doi.org/10.1029/2023GL107478, 2024.

Reddy, P. J., Perkins-Kirkpatrick, S. E., Ridder, N. N., and Sharples, J. J.: Combined role of ENSO and IOD on compound drought and heatwaves in Australia using CMIP6 large ensembles, Weather Clim. Extrem., 37, 100469, https://doi.org/10.1016/j.wace.2022.100469, 2022.

Seviour, W. J. M., Finkel, J., Rupp, P., Mudhar, R., Butler, A. H., Garfinkel, C. I., Hitchcock, P., Ayarzagüena, B., Hong, D.-C., Hyun, Y.-K., Kim, H., Lim, E.-P., De Maeseneire, D., Messori, G., Koren, G., Sigmond, M., Simpson, I. R., and Son, S.-W.: Forecast-based attribution of the role of stratospheric variability in weather extremes, EGUsphere, 2026,

https://doi.org/10.5194/egusphere-2026-4971
Preprint. Discussion started: 8 September 2026

1–28, https://doi.org/10.5194/egusphere-2026-230, 2026.

Shen, X., Wang, L., and Osprey, S.: Tropospheric forcing of the 2019 Antarctic sudden stratospheric warming, Geophys. Res. Lett., 47(20), e2020GL089343, https://doi.org/10.1029/2020GL089343, 2020.

Smith, K. L., and Kushner, P. J.: Linear interference and the initiation of extratropical stratosphere-troposphere interactions, J. Geophys. Res. Atmos., 117, D13107, https://doi.org/10.1029/2012JD017587, 2012.

Taguchi, M.: Predictability of major stratospheric sudden warmings: analysis results from JMA operational 1-month ensemble predictions, J. Atmos. Sci., 73(2), 789–806, https://doi.org/10.1175/JAS-D-15-0201.1, 2016.

Voldoire, A., Saint-Martin, D., Sénési, S., Decharme, B., Alias, A., Chevallier, M., Colin, J., Guérémy, J.-F., Michou, M., Moine, M.-P., Nabat, P., Roehrig, R., Salas y Mélia, D., Séférian, R., Valcke, S., Beau, I., Belamari, S., Berthet, S., Cassou, C., Cattiaux, J., Deshayes, J., Douville, H., Ethé, C., Franchistéguy, L., Geoffroy, O., Lévy, C., Madec, G., Meurdesoif, Y., Msadek, R., Ribes, A., Sanchez-Gomez, E., Terray, L., and Waldman, R.: Evaluation of CMIP6 DECK experiments with CNRM-CM6-1, J. Adv. Model. Earth Syst., 11(7), 2177–2213, https://doi.org/10.1029/2019MS001683, 2019.

Wang, Y., Rao, J., Lu, Y., Ju, Z., Yang, J., and Luo, J.: A revisit and comparison of QBO disruption events in 2015/16 and 2019/20, Atmos. Res., 294, 106970, https://doi.org/10.1016/j.atmosres.2023.106970, 2023.

Weinberger, I., Garfinkel, C. I., White, I. P., and Birner, T.: The efficiency of upward wave propagation near the tropopause: importance of refractive index form, J. Atmos. Sci., 78(8), 2605–2617, https://doi.org/10.1175/JAS-D-20-0267.1, 2021.

Williams, K. D., Harris, C. M., Bodas-Salcedo, A., Camp, J., Comer, R. E., Copsey, D., Fereday, D., Graham, T., Hill, R., Hinton, T., Hyder, P., Ineson, S., Masato, G., Milton, S. F., Roberts, M. J., Rowell, D. P., Sanchez, C., Shelly, A., Sinha, B., Walters, D. N., West, A., Woollings, T., and Xavier, P. K.: The Met Office Global Coupled model 2.0 (GC2) configuration, Geosci. Model Dev., 8(5), 1509–1524, https://doi.org/10.5194/gmd-8-1509-2015, 2015.

https://doi.org/10.5194/egusphere-2026-4971
Preprint. Discussion started: 8 September 2026